Efficient velocity model evaluation: 2D and 3D field data tests

Adam Halpert

ABSTRACT

Interpretation tools like image segmentation allow for fast generation of velocity models, but evaluating them can be computationally demanding. Previous work has shown the effectiveness of using Born-modeled synthesized wavefields to image targeted locations for this purpose, but only on synthetic data. Here, the model evaluation method is successfully demonstrated on both a 2D line and small 3D cube taken from a wide-azimuth field survey. The importance of a quantitative measure of focusing or image quality is also shown, especially for five-dimensional datasets that are difficult to visualize and judge qualitatively.

INTRODUCTION

In recent years, model-building bottlenecks have shifted from being computational or imaging-related, toward interpretation and other human-intensive tasks. This can be attributed to significant increases in computing power, without accompanying advances in interpretation tools or workflow processes. However, there is an opportunity to not only reduce the magnitude of this bottleneck, but to also take advantage of increased computational capability as it relates to model building. Instead of determining a single, "best-fit" model to use as the basis of imaging, it may be feasible to create a range of models, based on different geological scenarios. This can be especially useful for salt interpretation workflows; because of the high velocity contrast between salt and sediments, mis-placed or mis-interpreted salt bodies can have a disproportionately negative impact on subsalt images. While tools such as seismic image segmentation (Lomask et al., 2007; Halpert, 2013) can help provide these models, a way to efficiently test them is necessary in order to avoid costly and time-consuming re-migration of very large modern 3D datasets.

Quickly updating images based on discrete changes to the velocity model is a problem with several proposed solutions. Many proposals rely on a fast, target-oriented variant of beam migration (Hill, 1990); for example, Wang et al. (2008) update post-stack images to qualitatively judge the effects of using different velocity models. An alternative is to use a similar approach but with wave-equation methods like reverse-time migration (RTM) (Wang et al., 2011); however, this remains an extremeley expensive option. A different approach, first proposed by Halpert and Tang (2011), also employs wave equation imaging. However, by using an initial image and Born modeling (Stolt and Benson, 1986) to synthesize a new, targeted dataset (Tang and Biondi,

2010; Tang, 2011), the computational challenge is drastically reduced. Furthermore, if a pre-stack image with subsurface offset information is available, this method can make use of that information to identify and help correct errors in an initial velocity model. In Halpert (2012), initial tests using a 2D synthetic model were shown to be successful; here, I will present initial tests on 2D and 3D portions of a wide-azimuth field dataset. Using the field data, I will show that Born-synthesized wavefields can quickly discriminate between different velocity models, and quantitatively identify the most accurate of the options.

METHOD

The procedure for generating Born-modeled wavefields from an initial image was first outlined in Halpert and Tang (2011), and consists of three major steps:

1. Starting from an initial image, use a form of exploding reflector modeling to "record" an areal source function at a preferred datum.
2. Using the new source function and the initial image as a reflectivity model, synthesize a Born-modeled dataset (Tang, 2011) with arbitrary acquisition geometry suited to the imaging target(s).
3. Now, the synthesized source and receiver wavefields can be imaged conventionally, using any velocity model under consideration. New images can be produced using only a single shot, a substantial computational savings over re-migrations of the full dataset.

Areal source function

The areal source function is generated by first mapping subsurface offset information from a prestack image m onto its equivalent zero-offset positions, and performing exploding reflector modeling to record the source function at a user-specified datum. Choosing a datum deeper in the subsurface could lead to significant computational savings if the "target" for this procedure is very deep or below salt. The source function $S(\mathbf{x}_s, \omega)$, recorded at $\mathbf{x}_s = (x_s, y_s, z_s)$ can be represented as

$$S(\mathbf{x}_s, \omega) = \sum_{\mathbf{x}'} \sum_{\mathbf{h}} G^*(\mathbf{x}' - \mathbf{h}, \mathbf{x}_s, \omega) m(\mathbf{x}', \mathbf{h}), \tag{1}$$

where $\mathbf{h}$ is the vector of subsurface half-offsets; ω is angular frequency; and G is the Green's function propagating the wavefield to the receiver locations (here, * denotes the adjoint). For this step and all subsequent ones, crosstalk issues are avoided by selecting only isolated locations along an interpreter-selected horizon.

Born-modeled wavefields

The Born-modeled dataset d' is recorded it at arbitrary receiver locations $\mathbf{x}_r$:

$$d'(\mathbf{x}_r, \omega) = \sum_{\mathbf{x}'} \sum_{\mathbf{h}} \Gamma(\mathbf{x}_s, \mathbf{h}, \omega) G(\mathbf{x}' + \mathbf{h}, \mathbf{x}'_r, \omega) m(\mathbf{x}', \mathbf{h}). \tag{2}$$

Here, m is the reflectivity model (in our case, the isolated regions from the initial image), and the Γ term is defined as

$$\Gamma(\mathbf{x}_s, \mathbf{h}, \omega) = \sum_{\mathbf{x}_s} S(\mathbf{x}_s, \omega) G(\mathbf{x}_s, \mathbf{x}' - \mathbf{h}, \omega), \tag{3}$$

where S is the source function described in step 1. Because the velocity model used to compute the Green's functions is the same one used to generate the initial image, the resulting Born-modeled wavefield $d'(\mathbf{x}'_r, \omega)$ will be kinematically invariant regardless of the initial model (Tang, 2011). This is important for the goal of correcting inevitable errors in the initial velocity model.

Imaging with multiple models

Now, the synthesized areal source function and receiver wavefield can be imaged via standard downward continuation migration:

$$m'(\mathbf{x}', \mathbf{h}) = \sum_{\omega} G^*(\mathbf{x}' - \mathbf{h}, \omega) \sum_{\mathbf{x}_r} G^*(\mathbf{x}' + \mathbf{h}, \mathbf{x}'_r, \omega) d'(\mathbf{x}_r, \omega). \tag{4}$$

At this point, the Green's functions can be computed using *any* velocity model. In this way, a potential model can be tested using only a single shot – an enormous computational savings.

Image quality measure

In Halpert and Tang (2011), a simple quantitative measure of image quality was also introduced. By calculating the proportion of energy existing at or near zero-subsurface offset, the F measure below can quickly give an indication of the relative accuracy of different velocity models:

$$F = \frac{\sum_{i=\mathbf{p}} |A_i|}{\sum_{i=\mathbf{p}} |A_i| \exp\left(\alpha \frac{|h_i|}{h_{\max}}\right)}, \tag{5}$$

where $\mathbf{p}$ is the set of all image points, A_i is the amplitude at a given point, h_i is the subsurface offset at that point, and α is an optional user-specified weighting parameter. Using this measure, a value of $F = 1$ means that all energy is perfectly

Migration model	F value
Provided velocity	0.89
Fast model	0.86
Slow model	0.85

Table 1: Calculations from equation 5 for each 2D migration velocity model, after the initial image and synthesized wavefields were created using the provided velocity model.

focused at zero offset; as F decreases toward zero the image becomes progressively less focused. Ideally, a measure such as this one would allow a more rigorous comparison among possible models when a more qualitative comparison fails to yield an obvious result. In addition, a quantitative measure can be especially useful when evaluating five-dimensional images, which are extremely difficult to visualize.

2D RESULTS

The 2D and 3D images used to demonstrate this method are derived from a wide-azimuth Gulf of Mexico dataset provided by WesternGeco. Figure 1(a) is a 2D migration of a portion of this dataset, imaged using the velocity model provided with the data. To test the method, a single location along the reflector highlighted in Figure 1(b) was isolated and used to synthesize the source and receiver wavefields as described previously.

Figure 2 shows the results of imaging the new, synthesized wavefields with three different velocity models: the one provided with the data, and models scaled +/- 5% from the one provided. A qualitative examination suggests that the provided model produces the best-focused image, seen in panel (b). A more quantitative analysis using equation 5 confirms this; the F-values calculated for each of the images in Figure 2 are found in table 1.

A more interesting test case is one in which the initial image was not generated using the provided velocity model. The image in Figure 3(a) was created using the slower velocity model of the previous example; a location isolated from the reflector indicated in Figure 3(b) was used to synthesize the new source and receiver wavefields. The same reflector is chosen in Figure 3(b) as in Figure 1(b), although the location is slightly shifted due to the difference in velocity models. Now, Figure 4 shows the results of imaging the synthesized wavefields from this initial image, with the same three models as the previous example. Again, the provided model (panel b) delivers the most well-focused result, both qualitatively and quantitatively (from the F-value results in table 2). This demonstrates that the method can identify a more accurate model using field data, even when the initial model is less accurate.

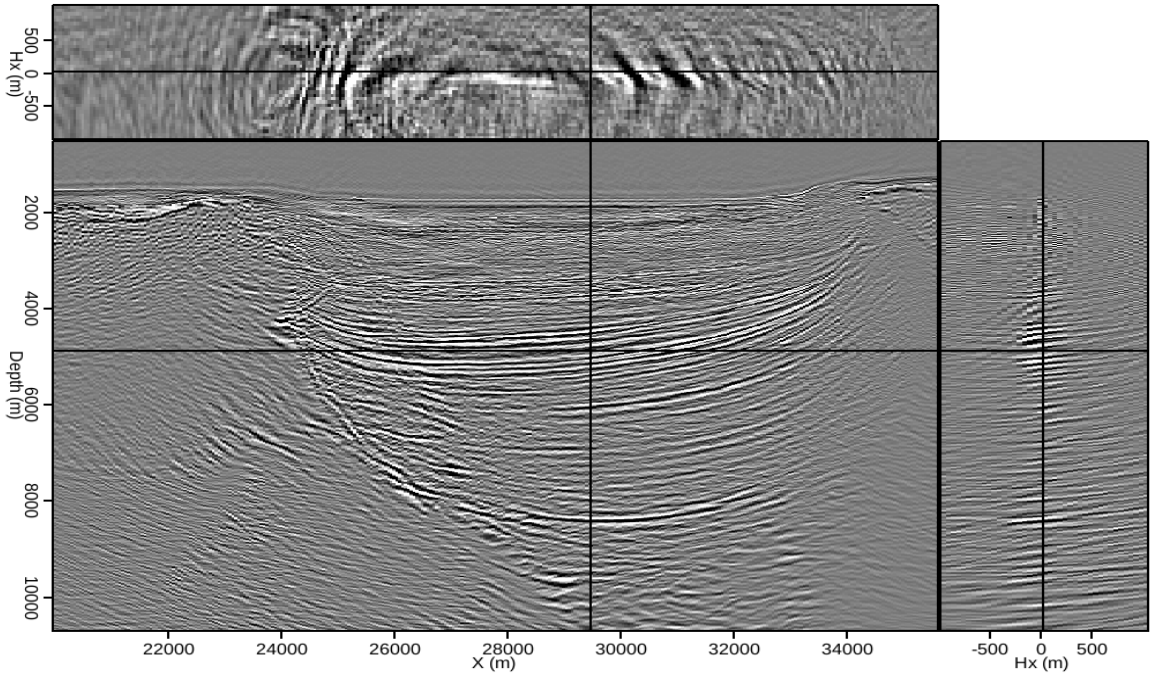

(a)

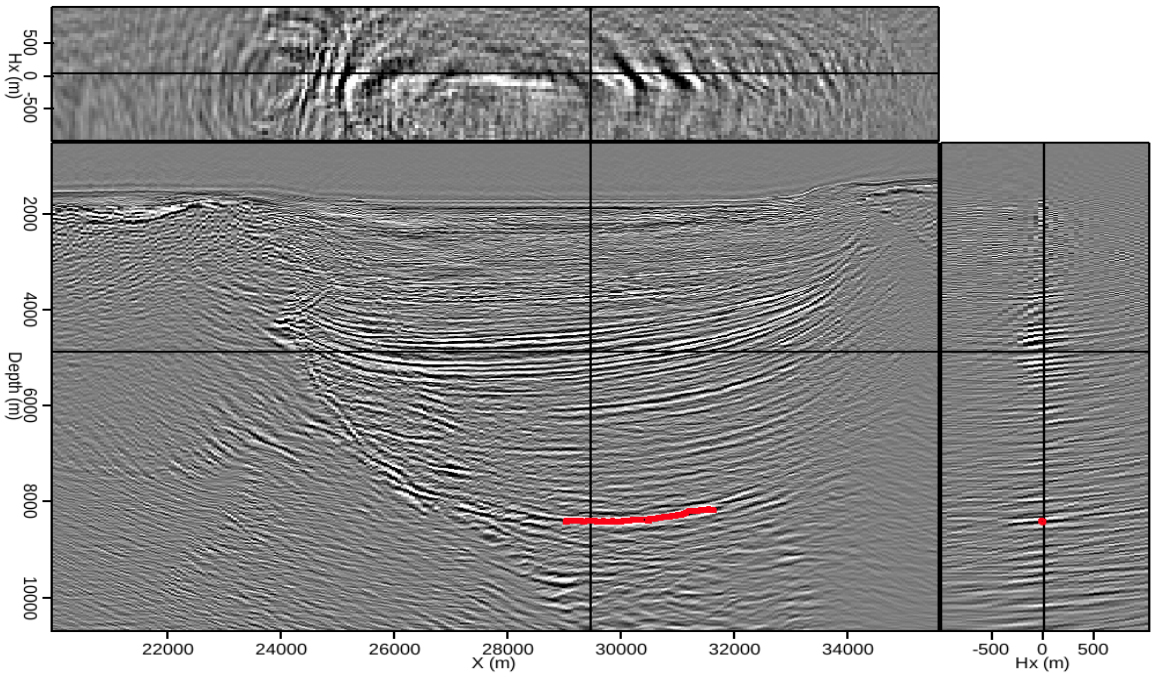

(b)

Figure 1: (a) A 2D field image produced using the provided velocity model, and (b) a manually-picked horizon of interest used to test three different velocity models. [**CR**]

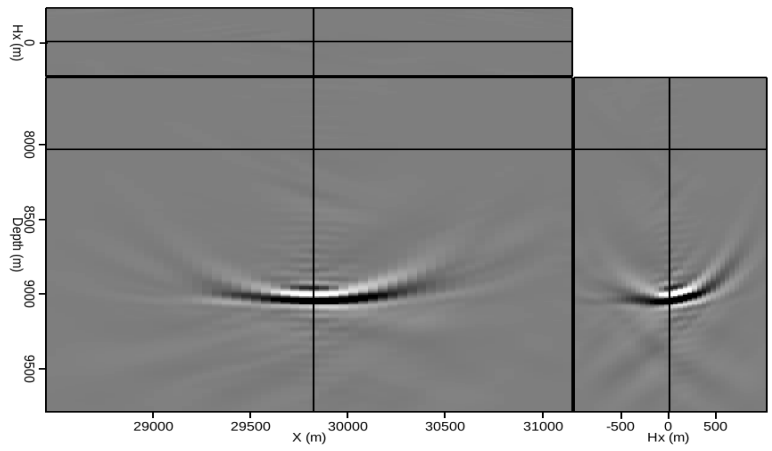

(a)

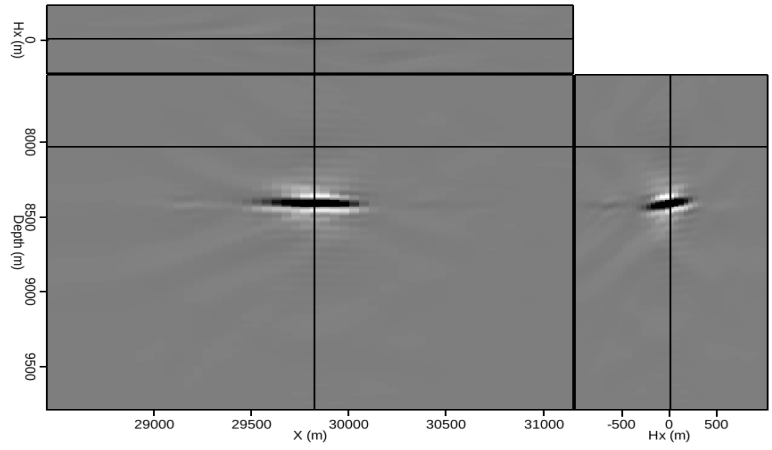

(b)

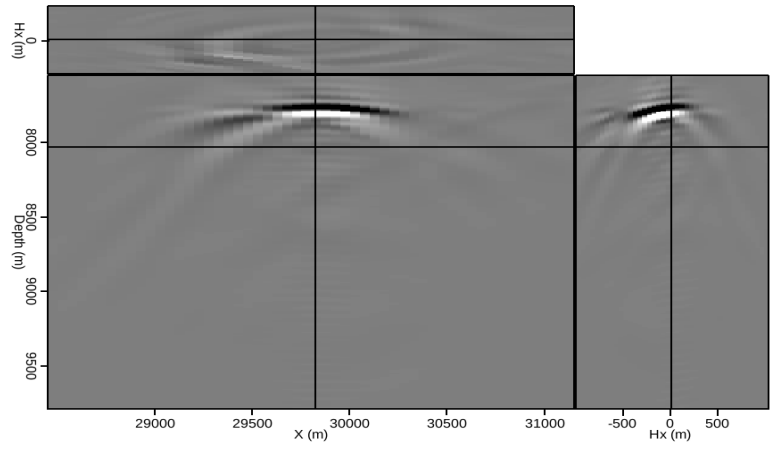

(c)

Figure 2: A single location from the reflector indicated in Figure 1(b), imaged using synthesized source and receiver wavefields and (a) a velocity model 5% faster than the one provided; (b) the provided velocity model; and (c) a model 5% slower than the one provided. [**CR**]

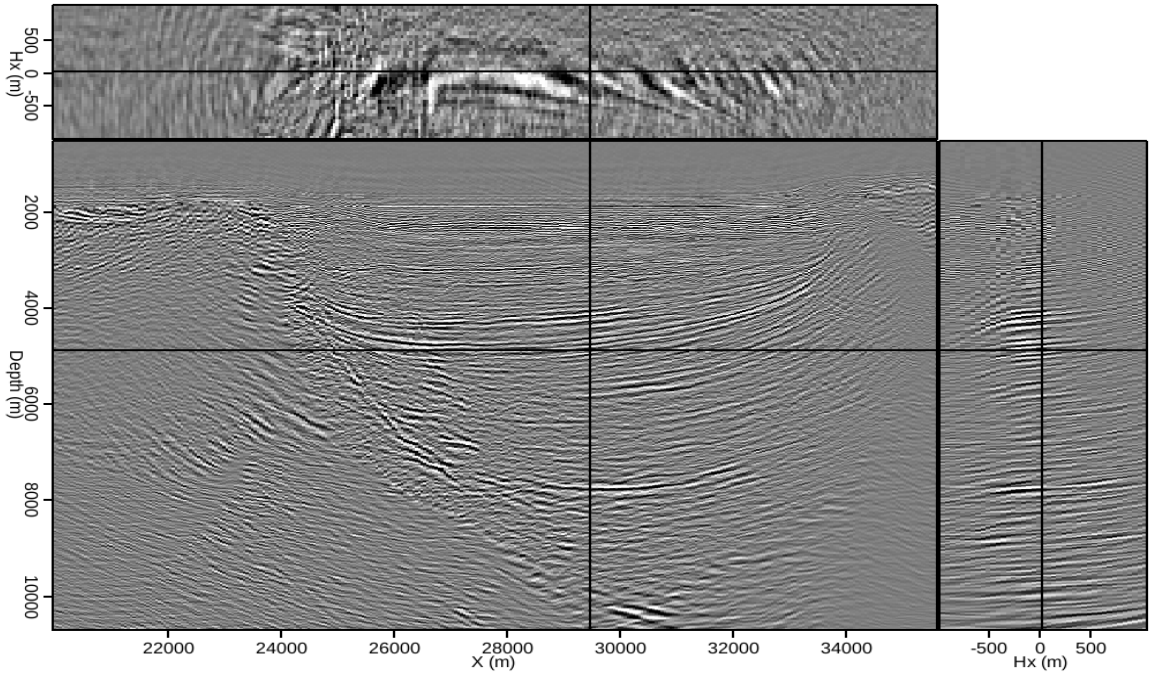

(a)

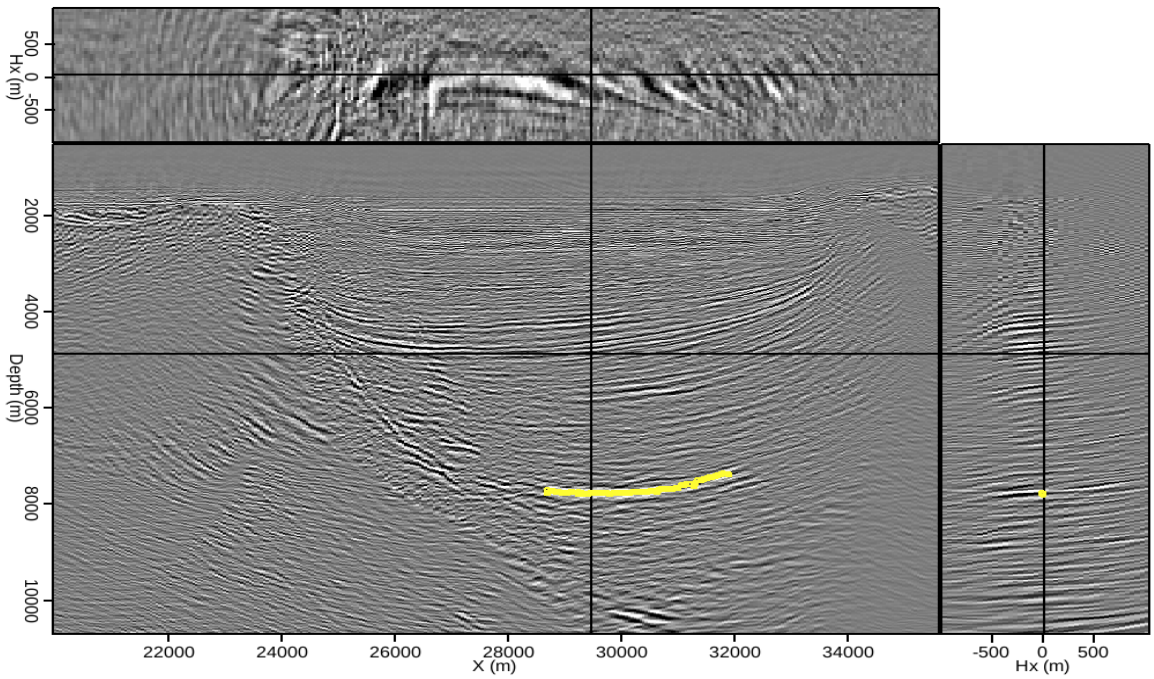

(b)

Figure 3: (a) A 2D field image produced using a velocity model 5% slower than the one provided, and (b) a manually-picked horizon of interest used to test three different velocity models. [**CR**]

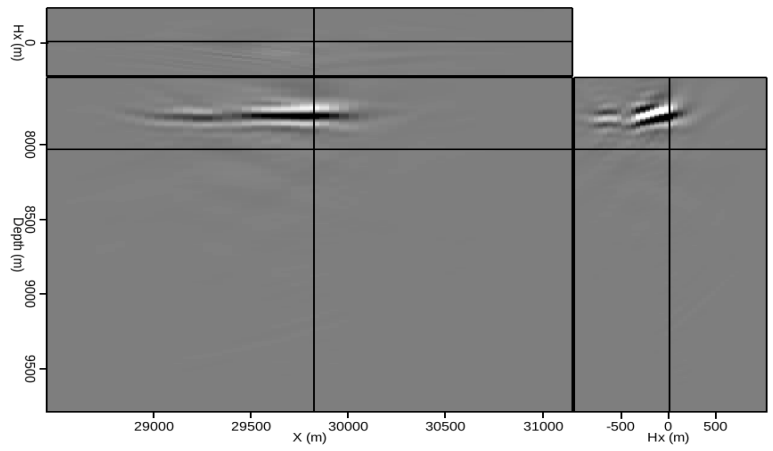

(a)

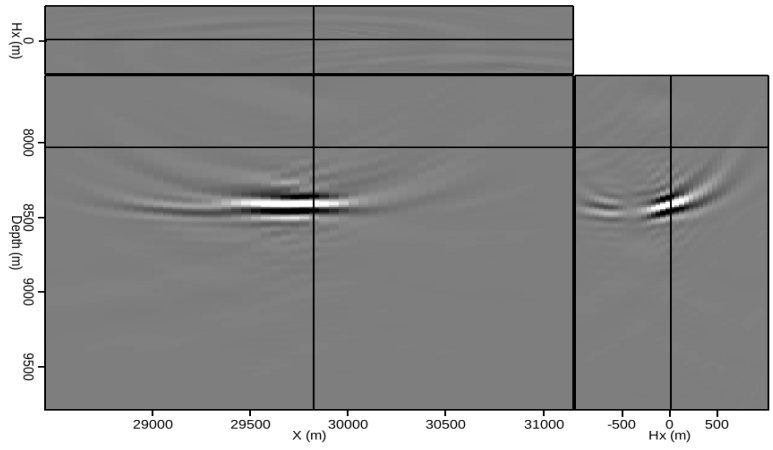

(b)

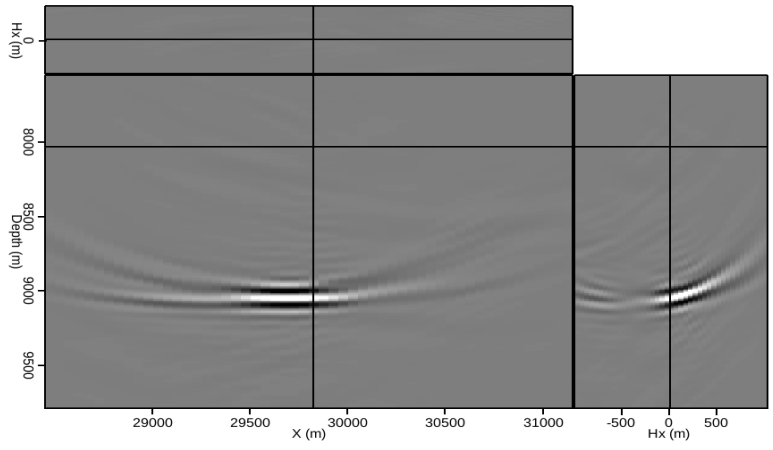

(c)

Figure 4: A single location from the reflector indicated in Figure 3(b), imaged using synthesized source and receiver wavefields and (a) a velocity model 5% slower than the one provided; (b) the provided velocity model; and (c) a model 5% faster than the one provided. [**CR**]

Migration model	F value
Provided velocity	0.92
Fast model	0.89
Slow model	0.89

Table 2: Calculations from equation 5 for each 2D migration velocity model, after the initial image and synthesized wavefields were created using a model 5% slower than the one provided.

Migration model	F value
Provided velocity	0.550
Fast model	0.514
Slow model	0.518

Table 3: Calculations from equation 5 for each 3D migration velocity model, after the initial image and synthesized wavefields were created using the velocity model provided with the data.

3D RESULTS

Finally, initial tests on 3D data were performed using the same strategy as in the previous section. Figure 5(a) shows a relatively small image cube derived from the same Gulf of Mexico dataset used for the 2D examples, and imaged using the provided velocity model. Again, a single location from the manually-interpreted reflector (this time, a 3D horizon) shown in Figure 5(b) was used to synthesize 3D areal source and Born-modeled receiver wavefields. Because the prestack image cubes resulting from the imaging of these wavefields are five-dimensional, the results are displayed as two separate figures. Figure 6 shows images extracted from the cube at zero-subsurface offset in both the x and y directions, after migrating the synthesized wavefields with the three velocity models used for the 2D examples. Figure 7 shows the corresponding images in subsurface offset coordinates, extracted at the indicated locations in Figure 6. In this example, the image generated using the provided velocity model (panel (b)) appears better focused in both domains. The 3D F-value calculations in table 3 provide more quantitative evidence.

The more realistic case of an initial image created using the faster velocity model also yielded encouraging results. While it is slightly more difficult to qualitatively distinguish the best-focused model either at zero-subsurface offset (Figure 9) or in the subsurface offset domain (Figure 10), the calculations in table 4 reveal that the provided model is indeed superior. This example demonstrates the value of a quantitative image focusing measure, especially for difficult-to-visualize 5D volumes.

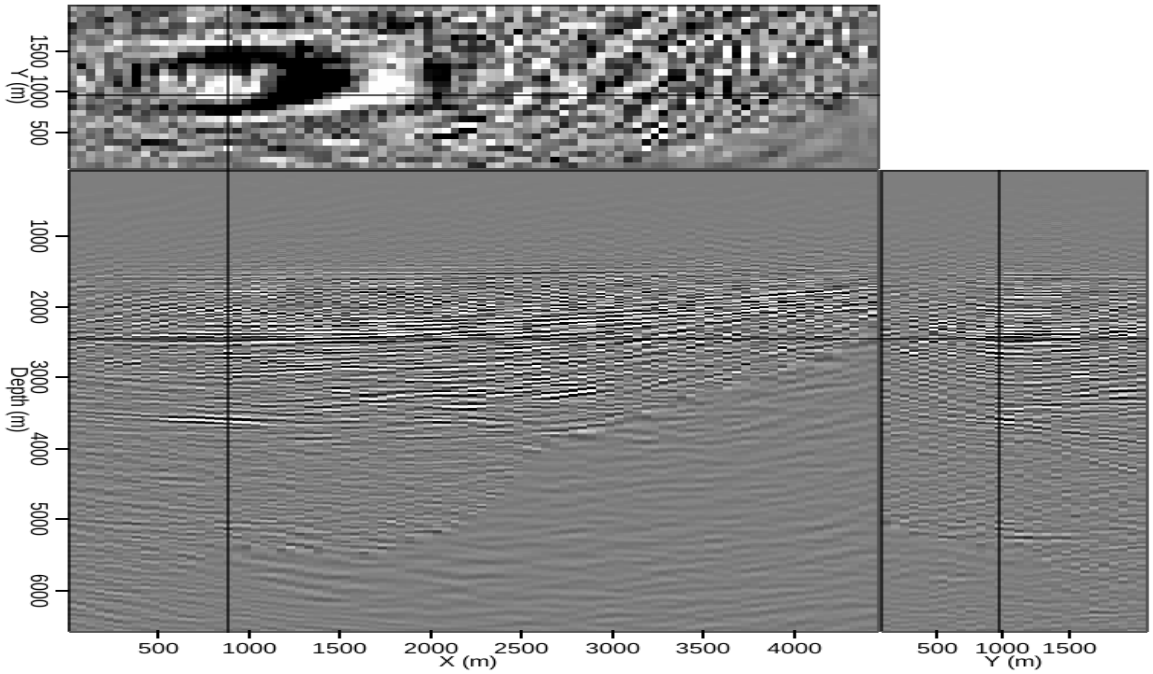

(a)

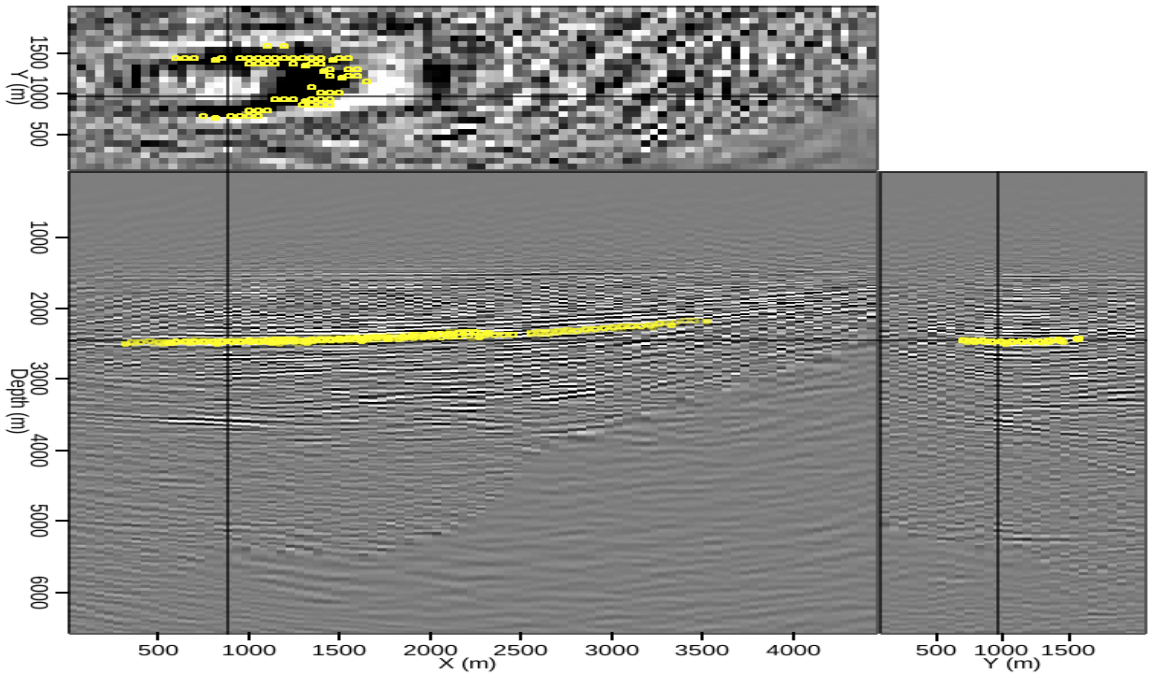

(b)

Figure 5: (a) A 3D field image produced using the provided velocity model, and (b) a manually-picked horizon of interest used to test three different velocity models. [**CR**]

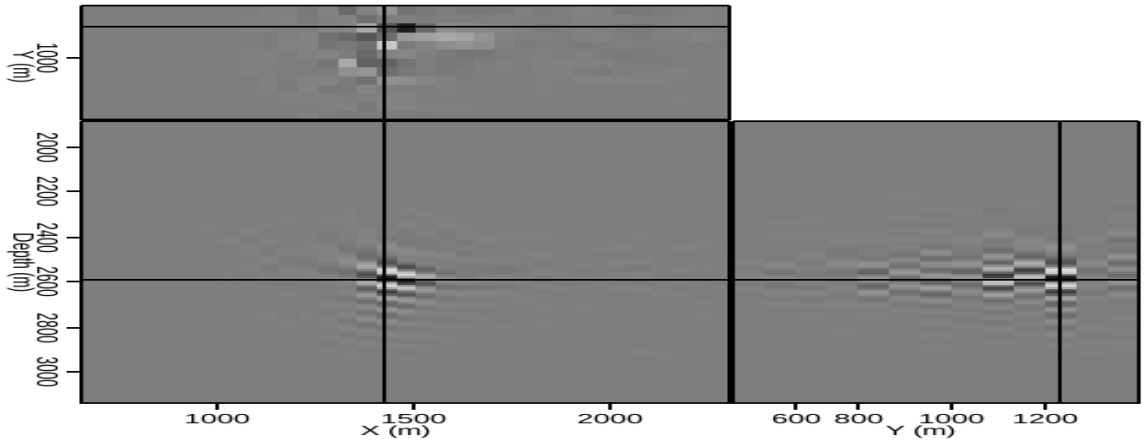

(a)

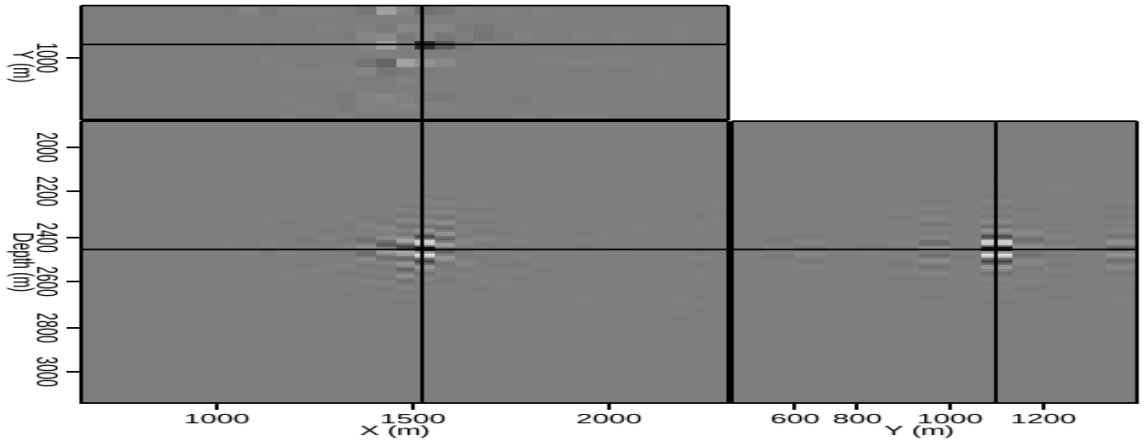

(b)

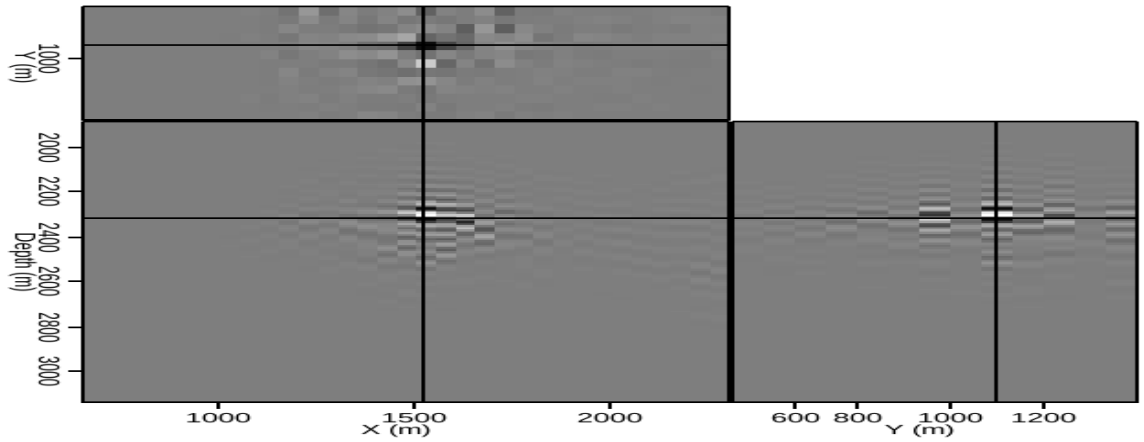

(c)

Figure 6: A single location from the reflector indicated in Figure 1(b), imaged using synthesized source and receiver wavefields and (a) a velocity model 5% faster than the one provided; (b) the provided velocity model; and (c) a model 5% slower than the one provided. [**CR**]

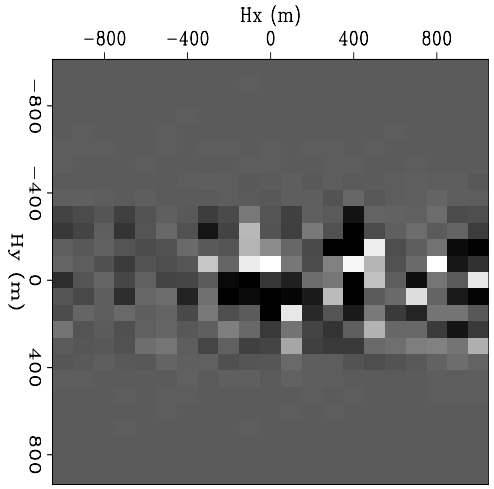

(a)

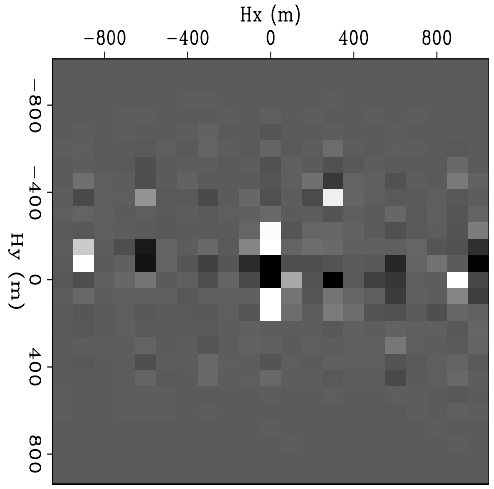

(b)

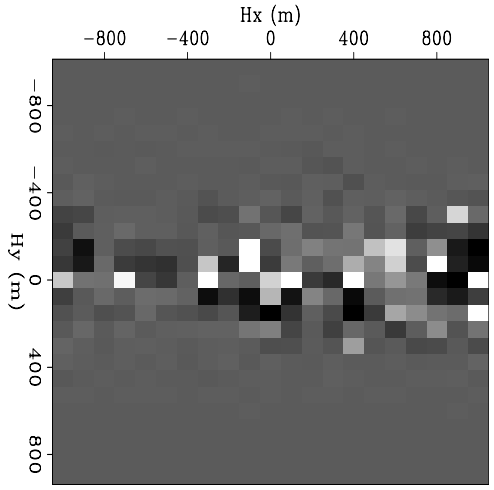

(c)

Figure 7: Subsurface offset images extracted from the indicated locations in Figure 6. The images were created using (a) the slower velocity; (b) the provided velocity; and (c) the faster velocity. [**CR**]

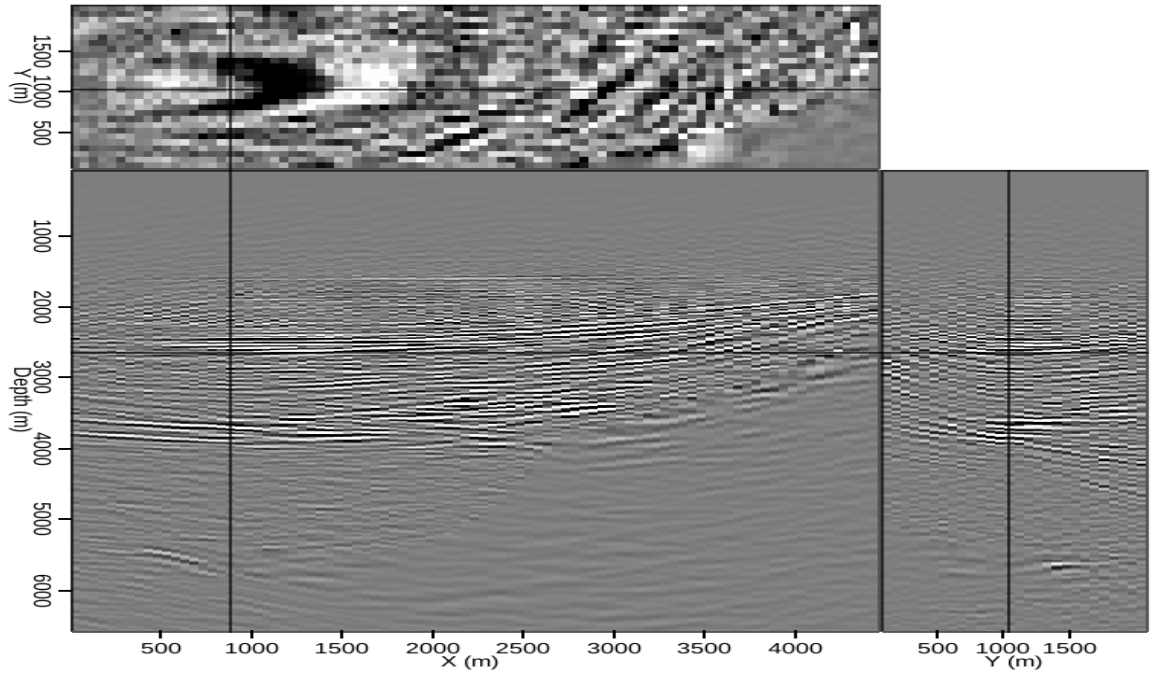

(a)

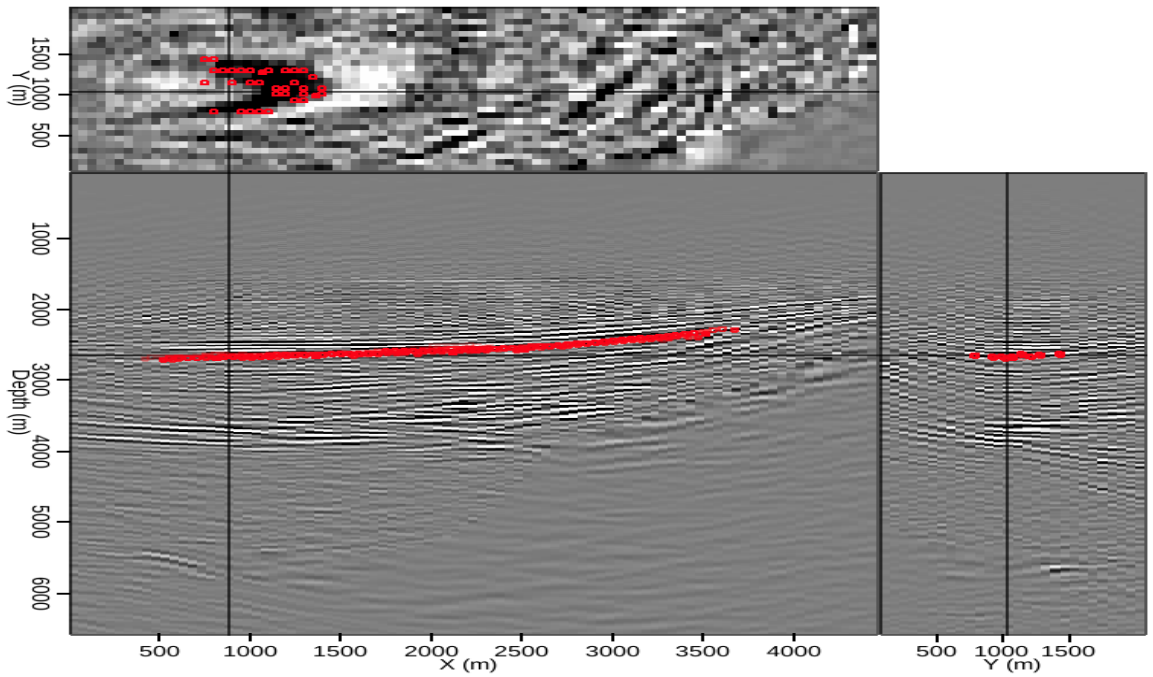

(b)

Figure 8: (a) A 3D field image produced using a velocity model 5% faster than the one provided, and (b) a manually-picked horizon of interest used to test three different velocity models. [**CR**]

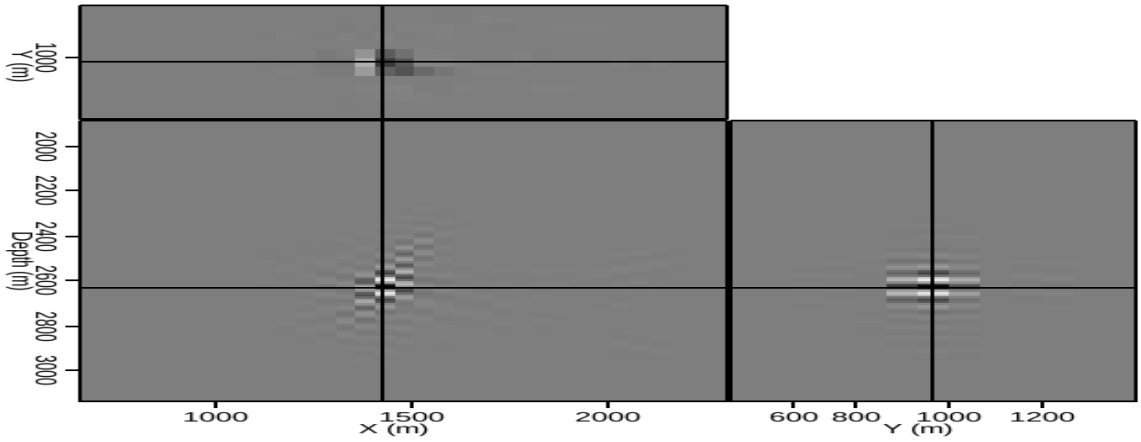

(a)

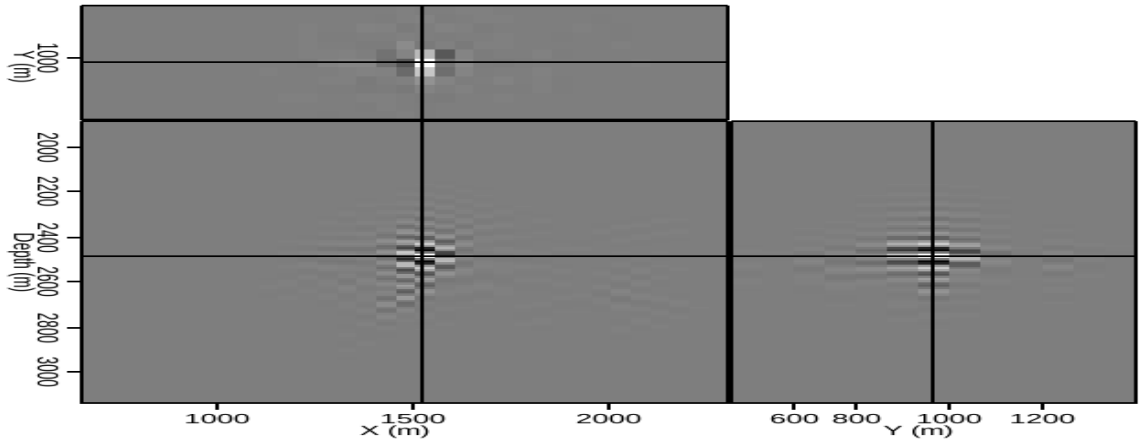

(b)

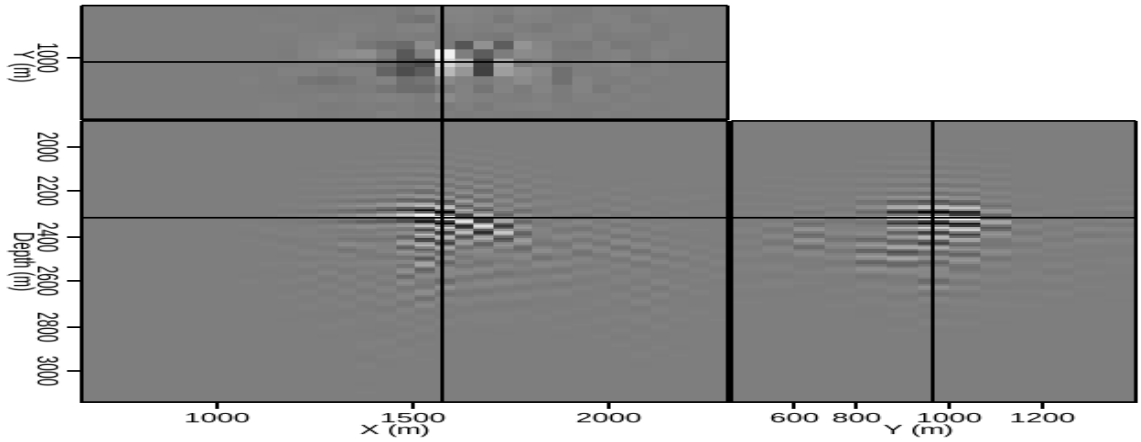

(c)

Figure 9: A single location from the reflector indicated in Figure 8(b), imaged using synthesized source and receiver wavefields and (a) a velocity model 5% faster than the one provided; (b) the provided velocity model; and (c) a model 5% slower than the one provided. [**CR**]

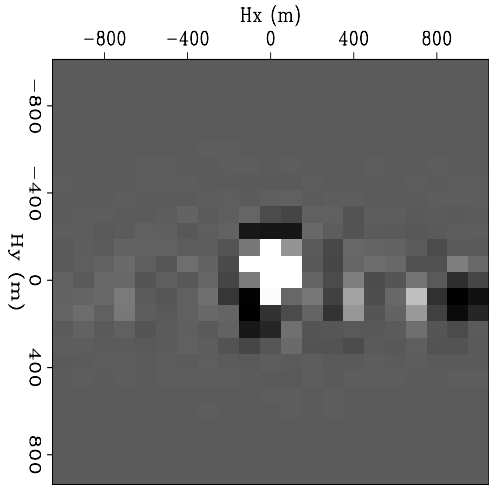

(a)

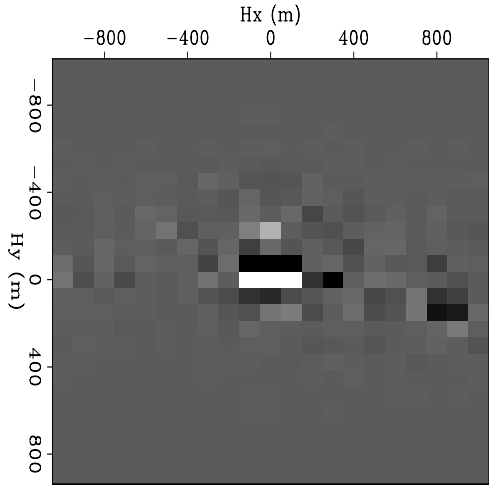

(b)

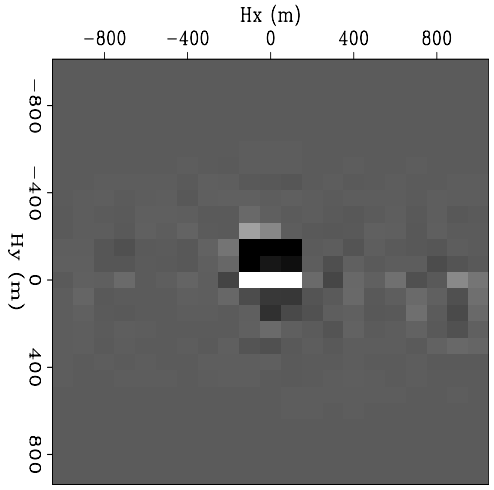

(c)

Figure 10: Subsurface offset images extracted from the indicated locations in Figure 9. The images were created using (a) the faster velocity; (b) the provided velocity; and (c) the slower velocity. [**CR**]

Migration model	F value
Provided velocity	0.481
Fast model	0.470
Slow model	0.466

Table 4: Calculations from equation 5 for each 3D migration velocity model, after the initial image and synthesized wavefields were created using a velocity model 5% faster than the one provided with the data.

CONCLUSIONS

The strategy of synthesizing areal source and Born-modeled receiver wavefields to efficiently test a range of possible velocity models, previously demonstrated only on synthetic data, has been successfully tested on 2D and 3D field data. By imaging only a single shot, the method can identify the most accurate model, even if the wavefields were synthesized using an inaccurate model. When used in conjuction with other computational interpretation tools such as image segmentation, this method may help to alleviate model-building and interpretation bottlenecks, especially when several feasible salt scenarios are under consideration.

ACKNOWLEDGMENTS

I am grateful to WesternGeco for providing the field dataset used here for examples, Yaxun Tang for his contributions to the Born modeling theory and framework, and to all SEP sponsors for their support.

REFERENCES

Halpert, A., 2012, Fast velocity model evaluation with synthesized wavefields: SEP-Report, **147**, 39–48.

———, 2013, Salt delineation via interpreter-guided 3D seismic image segmentation: SEP-Report, **149**, 107–120.

Halpert, A. and Y. Tang, 2011, Velocity model evaluation through Born modeling and migration: a feasibility study: SEP-Report, **145**, 15–26.

Hill, N. R., 1990, Gaussian beam migration: Geophysics, **55**, 1416–1428.

Lomask, J., R. G. Clapp, and B. Biondi, 2007, Application of image segmentation to tracking 3D salt boundaries: Geophysics, **72**, P47–P56.

Stolt, R. H. and A. Benson, 1986, Seismic migration: Theory and practice: Geophysical Press.

Tang, Y., 2011, Imaging and velocity analysis by target-oriented wavefield inversion: PhD thesis, Stanford University.

Tang, Y. and B. Biondi, 2010, Target-oriented wavefield tomography using demigrated Born data: SEP-Report, **140**, 67–82.

Wang, B., J. Ji, C. Mason, S. Gajawada, and Y. Kim, 2008, Beam-based interactive imaging for salt interpretation and salt model building: SEG Technical Program Expanded Abstracts, **27**, 3073–3077.

Wang, B., C. Mason, K. Yoon, J. Ji, J. Cai, S. Suh, and Z. Li, 2011, Complex salt model building using a combination of interactive imaging and layer-stripping RTM: First Break, **29**, 47–54.